Observation of collapse and revival of atomic four-wave mixing in Bose gases

Wei-Tao Wu [1,2] Zhi-Xin Duan [1,2] and Sheng-Jun Yang [1,2,3,*]

[1]*Shenzhen Institute for Quantum Science and Engineering, School of Science, Southern University of Science and Technology, Shenzhen 518055, China*

[2]*Guangdong Provincial Key Laboratory of Quantum Science and Engineering, Southern University of Science and Technology, Shenzhen 518055, China*

[3]*International Quantum Academy, Shenzhen 518048, China*

(Received 19 November 2023; revised 7 May 2024; accepted 28 May 2024; published 11 June 2024)

Atomic four-wave mixing (FWM) is an important nonlinear process in ultracold physics. Despite numerous works on atomic FWM, the phase coherence effect has not been extensively studied. Here, by preparing multiple spin-momentum modes with ultracold ^{87}Rb atoms in a crossed dipole trap and applying an external magnetic field to regulate the atomic motions and interactions, we extensively investigate how the coherence fluctuation affects the atomic FWM process. We observe that the atomic motion and spin-exchange collision involve a periodic collapse and revival of the yield fraction of the atomic FWM. The oscillation period is mainly determined by the spin-exchange rate and thus the atomic scattering cross section. Our work demonstrates that atomic FWM can be used to probe the coherence and the atomic interactions, which should benefit various areas related to multicomponent atomic interactions and spin dynamics in the future.

DOI: 10.1103/PhysRevA.109.063316

I. INTRODUCTION

The study of multicomponent ultracold atoms, including various degrees of freedom and different isotopes or elements, is an active research frontier, allowing us to explore many novel phenomena and applications in precision measurement [1–3], quantum simulation [4–7], and quantum information processing [8,9]. Interatomic interactions among these atoms play critical roles in all these applications. Well known is the binary atomic spinor collisions [10–16] in generating sub-Poissonian quantum correlations, namely, spin squeezing and entanglement [17,18], which surpass the standard quantum limit [19,20]. Furthermore, atom fragmentations with additional separable momenta enrich more research areas such as synthetic topological phases [5,6], nonequilibrium quantum dynamics [4,15], artificially created gauge symmetries and superfluidity [21–23], and gravity tests [24,25]. Recently, mass-imbalanced atomic mixtures and cold molecules realized with either bosons or fermions [26,27] have provided a far more fascinating platform for simulations involving strong-coupling phenomena and many-body dynamics [28–30].

In these multicomponent ultracold atoms, there usually exist strong many-body interactions. Coherence among these components will provide the interaction enhancement, leading to various nonlinear effects and unexpected modifications to the state evolution. In particular, nonlinear atomic four-wave mixing (FWM) has been observed since the early stages of ultracold physics [12,31–37]. Whether the nonlinear FWM effect exists or not should be taken care of for the aforementioned research areas. Usually, atomic FWM can be divided into two categories, namely, spontaneous and stimulated atomic FWMs. Similar to the optical parametric down-conversion, spontaneous atomic FWM produces correlated pairs of scattered atoms via binary collisions. Output correlation modes have been observed in both spin states [12,31] and momentum states [32,33]. The stimulated atomic FWM [34–37] generates an initially empty output mode in the presence of one seed mode and two pump modes of the atoms. Parametric amplification of specific modes can be achieved by optical lattice modifications of the atomic dispersion [38–42]. In addition to the requirement of energy and momentum conservation, it is believed that phase coherence among the atoms is essential in nonlinear matter-wave mixing.

Here, similar to the collinear atomic FWM scheme [36], we prepare multiple spin-momentum modes of a ^{87}Rb Bose-Einstein condensate (BEC) and investigate the phase coherence influence on the FWM output mode in detail. We hold the atoms in a crossed optical dipole trap for a controllable duration and observe a periodic collapse and revival of the FWM output. We find that this is due to the trapped atomic motion and spin-exchange collision involving loss and recovery of the coherence. Our work demonstrates that the two-body interaction properties can be retrieved by measuring the atomic FWM output mode. It may be useful particularly for those interactions that cannot be measured directly.

II. EXPERIMENT

Our experimental setup is illustrated in Fig. 1(a). About 2×10^5 ultracold ^{87}Rb atoms with the initial state of $|F = 1, m_F = -1\rangle$ are trapped in a 1064-nm crossed optical dipole trap (ODT). The size of the atom cloud is about 28 μm and

*Contact author: yangsj@sustech.edu.cn

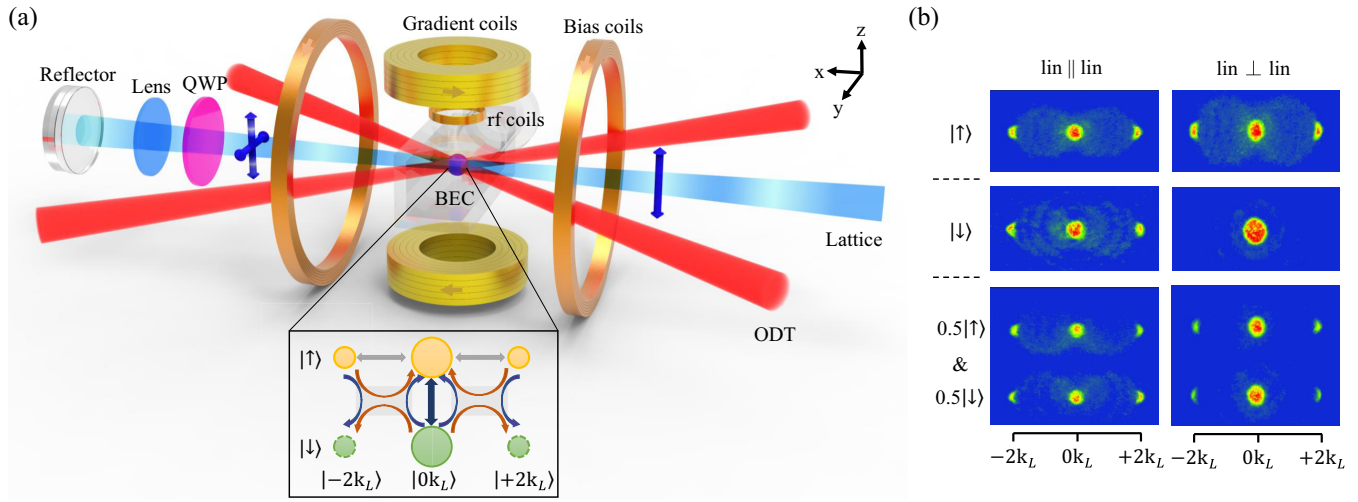

FIG. 1. (a) Scheme of the experimental setup and (b) momentum distribution images after the Kapitza-Dirac (KD) diffraction of various initial atomic states. (a) The BEC atoms are prepared in a 1064-nm crossed optical dipole trap (ODT), the bias and gradient coils generate the uniform and gradient magnetic fields at around the atoms separately, and the rf coils can transfer the atoms between the states $|F = 1, m_F = -1\rangle$ ($|\uparrow\rangle$) and $|1, 0\rangle$ ($|\downarrow\rangle$). One 771-nm laser beam propagates along the x axis and then is reflected to form a lattice for the KD diffraction of the momentum modes $|\pm 2k_L\rangle$, where k_L is the lattice wave vector. Polarization of the forward- and backward-propagating beams can be rotated to either parallel (lin∥lin) or orthogonal (lin⊥lin) by the quarter-waveplate (QWP), forming the spin-independent lattice or the spin-dependent lattice. The inset is a conceptual diagram of interactions involved in our system. The yellow and green circles represent the spin-momentum modes of the atoms. The black arrow between the zero-momentum spin states represents the spin-exchange collision. The gray arrows between the momentum modes represent the KD diffraction. The cured arrows represent the atomic FWM. (b) By applying the proper rf pulse, the atoms are initially prepared in the states of $|\uparrow\rangle$, $|\downarrow\rangle$, and evenly balanced ($0.5|\uparrow\rangle$ and $0.5|\downarrow\rangle$) from top to bottom. The momentum distribution images on the left and right sides correspond to the spin-independent and spin-dependent KD diffractions, respectively.

the atomic temperature is about 30 nK. The ODT is formed by an elliptical Gaussian laser beam that propagates horizontally (the xy plane). The laser beam is focused through the atoms in the $\hat{e}_-$ ($:=\hat{e}_x - \hat{e}_y$) direction and then refocused in the $\hat{e}_+$ ($:=\hat{e}_x + \hat{e}_y$) direction. The trapping frequencies $\{\omega_-, \omega_+, \omega_z\}$ of the three-dimensional (3D) dipole trap are $\{22.7, 31.4, 126.8\}$ Hz. A pair of bias coils along the x axis generate a constant magnetic field $B_0 \sim 10.35$ G to split the atomic ground states. A resonant radio-frequency (rf) pulse of frequency 7.24 MHz is used to rotate the atomic states between $|F = 1, m_F = -1\rangle$ and $|F = 1, m_F = 0\rangle$. Further transfer to the state $|F = 1, m_F = +1\rangle$ is effectively suppressed due to a large quadratic Zeeman shift. We define the two states $|F = 1, m_F = -1\rangle$ and $|F = 1, m_F = 0\rangle$ as the spin-up ($|\uparrow\rangle$) and spin-down ($|\downarrow\rangle$) states, forming a pseudospin-1/2 system.

A one-dimensional optical lattice, with wavelength $\lambda_L = 771$ nm, propagates through the atoms in the x direction. The beam waist is about 150 μm. Rotating the quarter waveplate, the forward- and backward-propagating beams can be tuned to be either linearly polarized or orthogonally polarized. The two different polarization settings are spin independent and spin dependent, respectively [43,44]. The spin-independent lattice (lin∥lin) means that the states $|\uparrow\rangle$ and $|\downarrow\rangle$ experience the same periodic potential. The spin-dependent lattice (lin⊥lin) means that only the state $|\uparrow\rangle$ experiences the periodic potential. Known as Kapitza-Dirac (KD) diffraction [45,46], a pulse of the lattice scatters atoms with momentum transfer at even multiples of the photon momentum. In the experiment, we apply the lattice pulse (the KD pulse) on the atoms to produce recoiling atoms in momentum modes $|\pm 2k_L\rangle$ ($k_L = 2\pi/\lambda_L$). Six spin-momentum modes of the atoms are obtained as shown in the inset of Fig. 1(a). We label them $|\alpha, lk_L\rangle$, where $\alpha = \{\uparrow, \downarrow\}$ and $l = \{-2, 0, +2\}$. Both of the $|\uparrow\rangle$ and $|\downarrow\rangle$ atoms are diffracted for the spin-independent lattice (lin∥lin), while only the $|\uparrow\rangle$ atoms are diffracted for the spin-dependent lattice (lin⊥lin).

Note that the spin-up state $|\uparrow\rangle$ is magnetic sensitive and the spin-down state $|\downarrow\rangle$ is magnetic insensitive; a gradient magnetic field can spatially separate them according to the Stern-Gerlach effect. We use the time-of-flight absorption imaging method to measure the atomic spin-momentum distribution. A pair of anti-Helmholtz coils, named the gradient coils as shown in Fig. 1(a), are used to generate the gradient field $B_{\rm SG}$ [$:=B'(x\hat{e}_x + y\hat{e}_y - 2z\hat{e}_z)$] around the atoms. Here B' is the gradient of the magnetic field. Immediately after the KD pulse, the ODT is switched off and a large gradient field $B_{\rm SG}$ is applied. After a freely expanding duration of 25 ms, the atoms with different spin and momentum states are well separated. We then optically pump all the atoms into the atomic cyclic state $|F = 2\rangle$ for absorption detection.

Figure 1(b) shows the absorption imaging after applying the spin-independent and spin-dependent KD diffractions on the atoms. From top to bottom, the atoms are initial prepared in the pure spin-up state ($|\uparrow\rangle$), the pure spin-down state ($|\downarrow\rangle$) and the half spin-up and half spin-down state ($0.5|\uparrow\rangle$ & $0.5|\downarrow\rangle$). The pulse width of the KD diffraction $\tau_{\rm KD}$ is set at 25 μs. The lattice potential $V_{\rm latt}$ is $4.5E_r$, where E_r is the recoil energy. When atoms are purely in the spin-up state, about 40% of the atoms are diffracted into the first momentum mode $|\pm 2k_L\rangle$ for both the spin-independent and spin-dependent lattices. When atoms are purely in the

spin-down state, the KD diffraction is identical for the spin-independent lattice and absent for the spin-dependent lattice. However, when both spin states exist, the spin-down nonzero-momentum modes $|\downarrow, \pm 2k_L\rangle$ appear as shown in the bottom right image of Fig. 1(b). If only considering the KD diffraction with the spin-dependent lattice, no atoms would exist in the modes $|\downarrow, \pm 2k_L\rangle$. The generation of the modes $|\downarrow, \pm 2k_L\rangle$ is due to the atomic FWM.

By using the spin-dependent KD diffraction, we perform a detailed study of the atomic FWM process and show how the phase coherence affects the yield fraction of the FWM. The inset of Fig. 1(a) presents a conceptual diagram of major interactions involved in our system. Initially, there exist four atomic modes $|\uparrow, 0k_L\rangle$, $|\uparrow, \pm 2k_L\rangle$, and $|\downarrow, 0k_L\rangle$, where $|\uparrow, \pm 2k_L\rangle$ are the seed modes and $|\uparrow, 0k_L\rangle$ and $|\downarrow, 0k_L\rangle$ are the pump modes. The output modes are $|\downarrow, \pm 2k_L\rangle$. Because of the symmetry of the KD diffraction, there are two exactly the same FWM processes for the modes $|\downarrow, +2k_L\rangle$ and $|\downarrow, -2k_L\rangle$. The curved arrows represent the atomic FWM process. We also plot the KD diffraction of the spin-up state with the gray arrows and the spin-exchange collision between the zero-momentum modes with the black arrow.

III. BASIC THEORY

Utilizing the slowly varying envelope approximation [47,48], the order parameter for the multicomponent Bose gases described by the Gross-Pitaevskii equation is a superposition $\sum_j \Psi_j$, where Ψ_j ($:=\psi_j e^{i(k_j r - E_j t/\hbar)}$) is the jth-component matter wave; $\hbar k_j$ and E_j ($:=\hbar^2 k_j^2/2M$) are the corresponding central momentum and kinetic energy, respectively; and ψ_j is the slowly varying amplitude, whose modulus is proportional to the atomic number N_j. Equations for ψ_j can be written as

$$\begin{aligned} i\hbar\partial_t\psi_j = &\left(-\frac{i\hbar^2 k_j}{M}\nabla - \frac{\hbar^2}{2M}\nabla^2 + U_j\right)\psi_j \\ &+ \sum_{lm} g_s \delta_{k_l - k_m}\delta_{E_l - E_m}\psi_l\psi_m^*\psi_j \\ &+ \sum_{lmn\,(\neq j)} g_s \delta_{k_l - k_m + k_n - k_j}\delta_{E_l - E_m + E_n - E_j}\psi_l\psi_m^*\psi_n, \quad (1) \end{aligned}$$

where M is the atomic mass, U_j is the external field potential for the component j, and $g_s = 4\pi\hbar^2 a_s/MV$, with a_s the s-wave scattering lengths and V the quantization volume. In addition, $\delta_{k_l - k_m}$, $\delta_{k_l - k_m + k_n - k_j}$, and $\delta_{E_l - E_m}$, $\delta_{E_l - E_m + E_n - E_j}$ are the Kronecker delta functions that satisfy the momentum and energy conservation. Nonzero interactions obey these phase-matching constraints and depend on the wave-packet overlap and coherence. The second term on the right-hand side is the self- and cross-phase modulations and the third term involves nonlinear wave mixing.

In our system, we denote the slowly varying envelope for each component by $\psi_{\alpha,\beta}$, where the spin $\alpha \in \{\uparrow, \downarrow\}$ and the momentum $\beta \in \{-2, 0, +2\}$ in units of k_L. Here N is the total atomic number. The spin-destruction interaction is ignored since it is much weaker than the spin-exchange interaction and the nonlinear wave mixing. Under the constraint of spin conservation, evolution of the FWM output modes can be written as

$$\begin{aligned} i\hbar\partial_t\psi_{\downarrow,\pm 2} = &\left(-\frac{\pm i2\hbar^2 k_L}{M}\nabla - \frac{\hbar^2}{2M}\nabla^2 + U_{\rm ODT}\right)\psi_{\downarrow,\pm 2} \\ &+ g_s\left(2\sum_\beta |\psi_{\downarrow,\beta} + \psi_{\uparrow,\beta}|^2 - |\psi_{\downarrow,\pm 2}|^2\right)\psi_{\downarrow,\pm 2} \\ &+ 2g_s(\psi_{\uparrow,0}\psi_{\downarrow,0}^* + \psi_{\downarrow,0}\psi_{\uparrow,0}^*)\psi_{\uparrow,\pm 2} \\ &+ 2g_s\psi_{\downarrow,\mp 2}\psi_{\uparrow,\mp 2}^*\psi_{\uparrow,\pm 2}, \quad (2) \end{aligned}$$

where $U_{\rm ODT}$ is the dipole trap potential. The first two terms on the right-hand side modify the atomic spatial distribution and the coherence phase. The last two terms are the atomic FWM. Since the separation speed of these components is proportional to their relative central momentum and the atoms are initially populated in the states $|\uparrow, 0k_L\rangle$, $|\uparrow, \pm 2k_L\rangle$, and $|\downarrow, 0k_L\rangle$, we eliminate the FWM process among the states $|\uparrow, \pm 2k_L\rangle$ and $|\downarrow, \pm 2k_L\rangle$. For a small time increment δt, the growth $|\delta\psi_{\downarrow,\pm 2}| \simeq 2g_s|(\psi_{\uparrow,0}\psi_{\downarrow,0}^* + \psi_{\downarrow,0}\psi_{\uparrow,0}^*)\psi_{\uparrow,\pm 2}|\delta t/\hbar$. The fraction of each component $f_{\alpha,\beta}$ is $\int |\psi_{\alpha,\beta}|^2 dV/N$, where N is the total atomic number and $\sum_{\rm all} f_{\alpha,\beta} = 1$. We decompose $\psi_{\alpha,\beta}$ as $\sqrt{n_{\alpha,\beta}}e^{i\theta_{\alpha,\beta}}$, where the density $n_{\alpha,\beta}$ and the phase $\theta_{\alpha,\beta}$ are functions of space and time. Upon squaring the equation and integrating over all space, we obtain

$$\delta f_{\downarrow,\pm 2} = \frac{16 g_s^2}{N\hbar^2}\int dV n_{\downarrow,0} n_{\uparrow,0} n_{\uparrow,\pm 2}\cos^2(\delta\theta_0)\delta t^2, \quad (3)$$

where $\delta\theta_0 = \theta_{\downarrow,0} - \theta_{\uparrow,0}$. Thus, variation and fluctuation of the atomic density and phase coherence of the spin mixture will influence the FWM output. Assuming the three components are initially overlapped with the same size, the separation time of the wave packets is about $R_{\rm TF}/v_R \simeq 2.3$ ms, where the Thomas-Fermi radius $R_{\rm TF} \simeq 14$ μm and the recoil velocity $v_R = 5.98$ mm/s in our system. The FWM process is finished within this separation time. In this work we make the initial wave packets of the three components overlap and focus on study how their phase coherence influences the atomic FWM. Recalling Eq. (2), modification of the phase coherence comes from the external field and atomic interactions. Before applying the spin-dependent KD pulse, we hold the zero-momentum spin states in an optical dipole trap $U_{\rm ODT}$ for a period of time. As experimentally demonstrated below, evolution of the two-component Bose gases induces local phase disturbances and thus modifies the FWM output fraction.

IV. COLLAPSE AND REVIVAL OF THE ATOMIC FWM OUTPUT

By initially holding two-component spinor atoms in a dipole trap $U_{\rm ODT}$, we demonstrate observation of a periodic collapse and revival of the atomic FWM output. We first use the $\pi/2$ rf pulse to prepare the BEC atoms equally distributed in the spin-up and spin-down states. The two spinor components are held in the dipole trap for a time duration of $t_{\rm h}$. Then the spin-dependent KD pulse is on to produce recoiling spin-up atoms in momentum modes $|\pm 2k_L\rangle$. Subsequently, the atomic FWM occurs. During these processes, no gradient magnetic field exists. Only a bias magnetic field B_0 is applied in the x direction. We measure the yield fraction

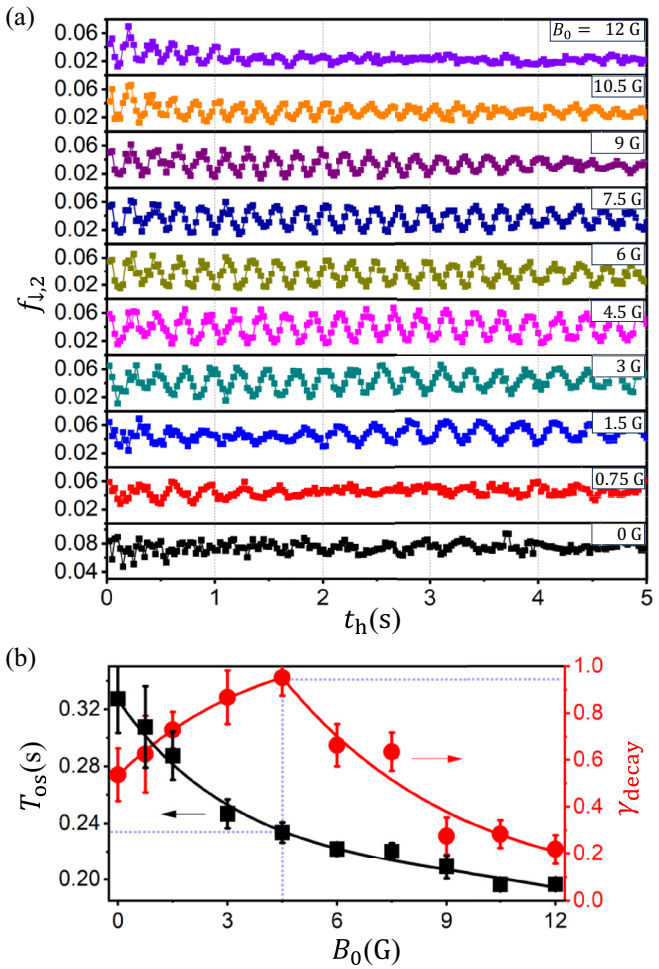

FIG. 2. Observation of the FWM output collapse and revival. (a) Oscillation of the yield fraction $f_{\downarrow,2}$ after a holding time t_h of the spin modes in the dipole trap. It is measured under different bias fields B_0 for comparison. (b) Oscillation period T_{os} (black squares) and amplitude attenuation γ_{decay} (red circles) of the fraction $f_{\downarrow,2}$ in (a). The data are fitted with growth and decay functions. The blue dotted line is to guide the eye for the case $B_0 = 4.5$ G.

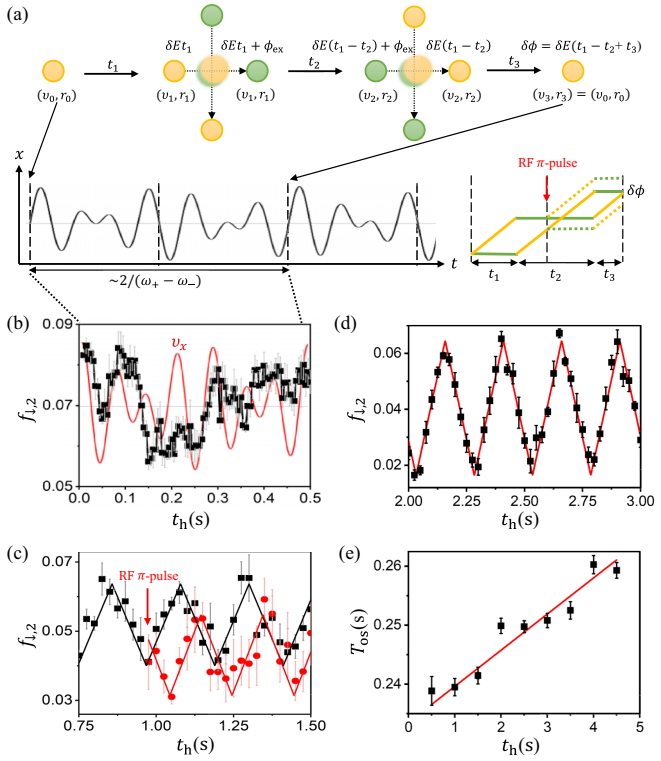

FIG. 3. (a) Conceptual diagram of atomic motion and spin-exchange collisions where v, r, and $\delta\phi$ are the atomic velocity, position, and phase shift, respectively. (b) Detail measurement of the output fraction $f_{\downarrow,2}$ when $B_0 = 0$ G and $t_h < 0.5$ s. The red line is the atomic velocity v_x corresponding to the example of atomic motion in (a). (c) Variation of $f_{\downarrow,2}$ by applying one rf π pulse at $t_h = 0.975$ s when $B_0 = 10.5$ G. (d) Example of the data fitting of Fig. 2(a) by using Eq. (4). Here $B_0 = 4.5$ G and 2 s $\leqslant t_h \leqslant$ 3 s. (e) Oscillation period T_{os} versus the holding time t_h when $B_0 = 4.5$ G. The linear fitting is to guide the eye.

$f_{\downarrow,2} = f_{\downarrow,+2} + f_{\downarrow,-2}$ when setting B_0 to various values ranging from 0 to 12 G during the holding time t_h. As shown in Fig. 2(a), $f_{\downarrow,2}$ oscillates as a function of the time t_h. When $B_0 = 0$ G, the value of $f_{\downarrow,2}$ is larger than the other cases due to the state degeneracy. We calculate the fraction oscillation period T_{os} and the amplitude attenuation γ_{decay} in Fig. 2(b). The T_{os} is the oscillation period in the beginning of t_h. It decreases with the increase of B_0. As discussed below, half of it equals the inverse of the spin-exchange rate η_{ex}. The γ_{decay} is defined as the ratio of the summed oscillation amplitude between the last and first half seconds of the holding time t_h, i.e., $\sum_{t_h=4.5\,s}^{5\,s} |f_{\downarrow,2} - \overline{f}_{\downarrow,2}| / \sum_{t_h=0\,s}^{0.5\,s} |f_{\downarrow,2} - \overline{f}_{\downarrow,2}|$, where $\overline{f}_{\downarrow,2}$ is the data average. The oscillation amplitude stays basically the same when $B_0 = 4.5$ G and decays at weak and strong magnetic fields.

In order to explain the observed phenomena, we discuss the behavior of the trapped atoms. The potential U_{ODT} is treated as a 3D harmonic trap, i.e., $\frac{1}{4}M\omega_-^2(x-y)^2 + \frac{1}{4}M\omega_+^2(x+y)^2 + \frac{1}{2}M\omega_z^2 z^2$. Since ω_z is large enough compared with $\omega_\pm$, we can simplify it as a two-dimensional horizontally planar trap. The harmonic motion for individual atom can be generally written as $r_+ \sin(\omega_+ t + \phi_+)(\hat{e}_x + \hat{e}_y) + r_- \sin(\omega_- t + \phi_-)(\hat{e}_x - \hat{e}_y)$, where $r_\pm$ and $\phi_\pm$ are determined by the atom's initial position and velocity. Since the FWM process deals with momentum modes on the x axis, we are concerned with atomic motion in this direction. We plot the oscillating position x in Fig. 3(a) when setting $r_+ = r_-$ and $\phi_+ = \phi_- = 0$. It roughly has a fast oscillation frequency $(\omega_+ + \omega_-)/2$ and a slow oscillation frequency $(\omega_+ - \omega_-)/2$. The atomic velocity and position change periodically and closely return to the atom's original state at a period of $2/(\omega_+ - \omega_-)$. The atomic motion induces local phase disturbances between the two spin states, thus influencing collective phase-matching conditions of the FWM process. In addition to the individual atomic motion, there also exist all kinds of atomic interactions. Among these interactions, the spin-exchange collision is the main factor that we need to discuss. Contributions of the other decoherence and dissipation factors such as spin destruction and inelastic scatterings are weak. The spin-exchange collision retains the original momentum state of the atom while flipping its inner spin state. As shown in Fig. 3(a), we illustrate the process by which one spin-up atom undergoes two

spin-exchange collisions at times t_1 and $t_1 + t_2$. During the collision, an extra phase ϕ_{ex} is created between the colliding atoms. The phase ϕ_{ex} is determined by the atomic wave vector k_v and the scattering cross section σ_{se}, i.e., approximately $-\arctan(k_v\sigma_{se})$. Its value is small and can be ignored in our experiment. Before and after the collision interaction, there is phase accumulation due to the energy difference δE between the two states. For an ensemble of atoms, the collisions occur with equal probability at any time if the atomic density is constant. This results in local phase disturbances. In addition, noise of the magnetic field B_0 also cause phase decoherence. After two collisions, the final phase shift $\delta\phi = \delta E(t_1 - t_2 + t_3)$ at time $T = t_1 + t_2 + t_3$. The $\delta\phi$ equals zero when $t_2 = t_1 + t_3$, and the total time $T = 2/\eta_{ex}$ on average. We treat the spin-exchange collision as a mirror, so the process can be likened to a $\pi/2$-π-π-$\pi/2$ interferometer [bottom right graph in Fig. 3(a)]. Considering both the atomic motion and the spin exchange, phase coherence is perfectly restored and the atom returns to its original state if the two characteristic times are equal, i.e., $2/\eta_{ex} = 2/(\omega_+ - \omega_-) \simeq 0.23$ s. The value is close to the oscillation period T_{os} at around $B_0 = 4.5$ G, as shown in Fig. 2(b). When η_{ex} is away from $\omega_+ - \omega_-$, the coherence cannot be restored and the attenuation γ_{decay} becomes fast. It is worth noting that there exists a disturbance on the initial output oscillation of $f_{\downarrow,2}$, as shown in Fig. 2(a). This disturbance should be attributed to atomic motion. It becomes smooth after several spin-exchange collisions as the accumulated phase difference of the atomic motion is averaged out. For a strong magnetic field and long holding time, spin-exchange-induced phase disturbances will play a major role.

To check the influence of atomic motion and spin exchange, we further carry out two measurements in Figs. 3(b) and 3(c). In Fig. 3(b) we set the magnetic field $B_0 = 0$ G and measure the first 0.5-s output fraction $f_{\downarrow,2}$ in more detail. Here, for comparison, we also plot the atomic velocity v_x as a red line corresponding to the example of atomic motion in Fig. 3(a). Since $B_0 = 0$ G, the two spin states are degenerate, i.e., $\delta E = 0$. Disturbance of $f_{\downarrow,2}$ is mainly determined by variation of atomic velocity. The positions of the local minimum and maximum value of $f_{\downarrow,2}$ are roughly consistent with the change of atomic velocity. Meanwhile, it can be seen that the value of $f_{\downarrow,2}$ has a slowly varying decay and recovery process with time. The $f_{\downarrow,2}$ gradually decreases as more and more atoms experience spin-exchange collisions that modify their velocities. It then increases as more and more atoms return to their original state after two collisions. For a strong magnetic field B_0, there exist a large phase shift $\delta E t$ and thus significant coherence fluctuations due to spin-exchange collisions. In Fig. 3(c) we set the magnetic field $B_0 = 10.5$ G and apply a rf π pulse to flip the atomic spin states at a minimum position $t_h = 0.975$ s. The rf π pulse is at the time $T/2$, as shown in the bottom right graph of Fig. 3(a). It will stop the phase shift $\delta\phi$ from returning to zero. As evidenced by experimental data in Fig. 3(c), $f_{\downarrow,2}$ continues to drop and then reverses at a later time. However, it is lower compared with the original maximum value.

From the above analysis and measurement, we can conclude that the collapse and revival oscillations mainly come from the atomic spin exchange. For simplicity, we only consider phase shift and disturbance induced by spin-exchange collisions. The fraction $f_{\downarrow,2}$ is the integral over the condensates, thus depending on the proportion of atoms involved in the spin-exchange collision. We get its evolution over the holding time t_h,

$$f_{\downarrow,2} = \mathcal{A}\left((1-\eta) + \eta\frac{|(t_h \mathrm{mod} T_{os}) - T_{os}/2|}{T_{os}/2}\right), \quad (4)$$

where $\mathcal{A}$ is the maximum output fraction and η is the destructive ratio of the FWM. We use this equation to fit the data in Fig. 2(a). Each fitting selects the experimental data within a 1-s time segment, as shown in Fig. 3(d), for example, where $B_0 = 4.5$ G and $2\ \mathrm{s} \leqslant t_h \leqslant 3$ s. The destructive ratio η is related to the degree of collective phase decoherence and therefore increases with B_0. Here we focus on the oscillation period T_{os}. The period T_{os} is mainly determined by the spin-exchange collision, i.e., $T_{os} = 2/\eta_{ex}$. The fitting results of T_{os} are shown in Fig. 2(b) for different B_0 and in Fig. 3(e) for different t_h. The T_{os} decreases with the magnetic field B [Fig. 2(b)], as the collision rate η_{ex} is proportional to the atomic cross section σ_{se}. Considering the atomic density $\rho \sim 1.25 \times 10^{13}$ cm^{-3} and the averaged velocity $v_{rms} \sim 1.69$ mm/s, we obtain $\sigma_{se} = \sqrt{2}\eta_{ex}/\rho v_{rms} = 2\sqrt{2}/\rho T_{os} v_{rms} = 5.75 \times 10^{-12}$ cm^2 when $B_0 = 4.5$ G. The corresponding atomic scattering length is about $90.4a_0$, where a_0 is the Bohr radius. It is in agreement with other measurements by looking at the temporal evolution of the atomic density profiles [49,50]. The period T_{os} increases for long holding time, as shown in Fig. 3(e). It is easy to understand because the atomic loss leads to a smaller atomic density and a lower collision rate.

V. THE FWM OUTPUT FOR DIFFERENT INITIAL ATOMIC DISTRIBUTIONS

In Sec. IV we demonstrated that the phase coherence plays an important role in the yield fraction $f_{\downarrow,2}$. However, as the KD diffraction and the FWM process are involved in succession after the holding time t_h, we need to figure out the specific influence of the coherence on each of them. Here the bias magnetic field B_0 is set at 10.5 G. We change the initial distributions of the states $|\uparrow, 0k_L\rangle$ and $|\downarrow, 0k_L\rangle$ by variation of the rf pulse. The yield fractions $f_{\downarrow,2}$ for different initial distributions $f^i_{\downarrow,0}$ are shown in Fig. 4(a). We compare three cases of the holding time $t_h = \{0, 0.14, 2.7\}$ s. The time $t_h = 0.14$ s corresponds to around the first minimum of the measured $f_{\downarrow,2}$ in Fig. 2(a). Times $t_h = 0$ and 2.7 s correspond to the initial stage and the stable stages separately. The gray curve in Fig. 4(a) is a theoretical function of $\mathcal{C} f^i_{\downarrow,0}(1 - f^i_{\downarrow,0})^2$, where the coefficient $\mathcal{C}$ is based on the maximum value measured in the case of $t_h = 0$ s. There are some discrepancies between the theory and experiment, since the function only simply considers the initial atomic proportion and ignores their modification during the FWM process.

In order to determine the respective effects of the KD diffraction and the FWM, we calculate the efficiency of the KD diffraction Θ_{KD} of the three cases in Fig. 4(b). Here Θ_{KD} is equal to $(f_{\downarrow,2} + f_{\uparrow,2})/(1 - f^i_{\downarrow,0})$. The presence of atoms in the state $|\downarrow\rangle$ reduces the effective lattice potential for the state $|\uparrow\rangle$ [51] and thus decreases the efficiency Θ_{KD} for large $f^i_{\downarrow,0}$. For the case of $t_h = 0.14$ s, the efficiency $\Theta_{KD} \simeq 0.4$

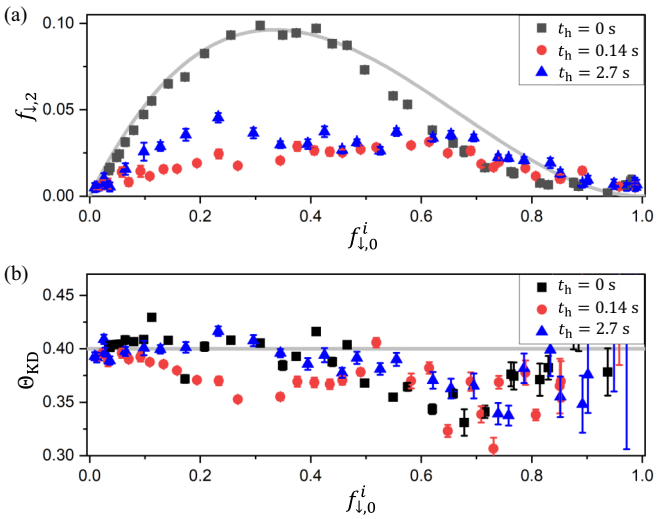

FIG. 4. Yield fraction $f_{\downarrow,2}$ versus the initial distribution $f^i_{\downarrow,0}$ of (a) the state $|\downarrow, 0k_L\rangle$ and (b) the corresponding KD diffraction efficiency Θ_{KD}. Three cases of the holding time $t_h = \{0, 0.14, 2.7\}$ s are shown for comparison. The theoretical curve in (a) is normalized to the maximum when $t_h = 0$ ms and the line in (b) corresponds to $\Theta_{KD} = 0.4$.

when $f^i_{\downarrow,0} < 0.1$. It gradually decreases from 0.4 as $f^i_{\downarrow,0}$ increases. As the spin-exchange rate η_{ex} is proportional to the atomic density, more atoms in the state $|\uparrow, 0\rangle$ will experience one spin-exchange collision for larger $f^i_{\downarrow,0}$. According to the $T_{os} \simeq 0.2$ s measured in Fig. 2(b), half of the spin-up atoms will be scattered around $f^i_{\downarrow,0} = 0.35$. Consistently, as shown by the red circles in Fig. 4(b), Θ_{KD} drops to a minimum when $f^i_{\downarrow,0} \simeq 0.3$. As $f^i_{\downarrow,0}$ further increases, most of the spin-up atoms experience one collision and phase coherence over all the spin-up atoms is restored. When increasing $f^i_{\downarrow,0}$ close to one or for long holding time, i.e., $t_h = 2.7$ s, all spin-up atoms have been through enough collisions. The phase difference over all the spin-up atoms will be averaged out. As confirmed in Fig. 4(b), Θ_{KD} is the same for the two cases of $t_h = 0$ and 2.7 s. Considering only variation of the value of the efficiency Θ_{KD} is not enough to lead to the yield attenuation of $f_{\downarrow,2}$. So we conclude that the observed collapse and revival of $f_{\downarrow,2}$ in Sec. IV is truly determined by the atomic FWM process instead of the KD diffraction. Our phenomenological model and analysis should be reasonable.

VI. CONCLUSION

In this work, by holding two-component atoms in an optical dipole trap and successively applying the KD diffraction to induce the atomic FWM, a periodic collapse and revival of the FWM output has been observed. We pointed out that it is due to local phase disturbances influenced by the atomic motion and spin-exchange collision during the dipole trap. A simple physical picture based on the individual atomic behavior was presented to explain these phenomena. By measuring the yield fraction, we obtained the two-body interaction parameters including the spin-exchange rate and the atomic scattering length. Future work may include isolating the effects of atomic motion and spin exchange, for example, by using the flat-topped beam trap, to achieve more accurate measurements. Comprehensive theoretical and experimental studies of these phenomena involving many-body interactions and various dissipations are worthwhile both for a deeper understanding and for potential measurement applications. During evolution of the two-component Bose gases, if external fields or other atoms or molecules are introduced to interact with one of the components, we may be able to detect these interactions according to the atomic FWM output. It is attractive to provide a zero-background measurement because the output atoms can be isolated and detected by the time-of-flight method. In conclusion, we have demonstrated that the atomic FWM is quite sensitive to phase coherence and can be used as a probe of ultracold atomic interaction and dynamical evolution, which may benefit various areas of research involving multicomponent matter waves.

ACKNOWLEDGMENTS

This work was supported by the Key-Area Research and Development Program of Guangdong Province through Grant No. 2019ZT08X324 and Guangdong Provincial Key Laboratory through Grant No. 2019B121203002.

[1] J. M. Higbie, L. E. Sadler, S. Inouye, A. P. Chikkatur, S. R. Leslie, K. L. Moore, V. Savalli, and D. M. Stamper-Kurn, Direct nondestructive imaging of magnetization in a spin-1 Bose-Einstein gas, Phys. Rev. Lett. **95**, 050401 (2005).

[2] T. Kinoshita, T. Wenger, and D. Weiss, A quantum Newton's cradle, Nature (London) **440**, 900 (2006).

[3] S. S. Kondov, C.-H. Lee, K. H. Leung, C. Liedl, I. Majewska, R. Moszynski, and T. Zelevinsky, Molecular lattice clock with long vibrational coherence, Nat. Phys. **15**, 1118 (2019).

[4] D. M. Stamper-Kurn and M. Ueda, Spinor Bose gases: Symmetries, magnetism, and quantum dynamics, Rev. Mod. Phys. **85**, 1191 (2013).

[5] N. Goldman, J. C. Budich, and P. Zoller, Topological quantum matter with ultracold gases in optical lattices, Nat. Phys. **12**, 639 (2016).

[6] T. Ozawa and H. M. Price, Topological quantum matter in synthetic dimensions, Nat. Rev. Phys. **1**, 349 (2019).

[7] F. Schafer, T. Fukuhara, S. Sugawa, Y. Takasu, and Y. Takahashi, Tools for quantum simulation with ultracold atoms in optical lattices, Nat. Rev. Phys. **2**, 411 (2020).

[8] C. Vo, S. Riedl, S. Baur, G. Rempe, and S. Dürr, Coherent logic gate for light pulses based on storage in a Bose-Einstein condensate, Phys. Rev. Lett. **109**, 263602 (2012).

[9] J. W. Park, Z. Z. Yan, H. Loh, S. A. Will, and M. W. Zwierlein, Second-scale nuclear spin coherence time of ultracold $^{23}Na^{40}K$ molecules, Science **357**, 372 (2017).

[10] M.-S. Chang, C. D. Hamley, M. D. Barrett, J. A. Sauer, K. M. Fortier, W. Zhang, L. You, and M. S. Chapman, Observation of spinor dynamics in optically trapped ^{87}Rb Bose-Einstein condensates, Phys. Rev. Lett. **92**, 140403 (2004).

[11] H. Schmaljohann, M. Erhard, J. Kronjäger, M. Kottke, S. van Staa, L. Cacciapuoti, J. J. Arlt, K. Bongs, and K. Sengstock, Dynamics of $F = 2$ spinor Bose-Einstein condensates, Phys. Rev. Lett. **92**, 040402 (2004).

[12] M. Chang, Q. Qin, W. Zhang, L. You, and M. Chapman, Coherent spinor dynamics in a spin-1 Bose condensate, Nat. Phys. **1**, 111 (2005).

[13] A. Widera, F. Gerbier, S. Fölling, T. Gericke, O. Mandel, and I. Bloch, Coherent collisional spin dynamics in optical lattices, Phys. Rev. Lett. **95**, 190405 (2005).

[14] G. Cappellini, M. Mancini, G. Pagano, P. Lombardi, L. Livi, M. S. de Cumis, P. Cancio, M. Pizzocaro, D. Calonico, F. Levi, C. Sias, J. Catani, M. Inguscio, and L. Fallani, Direct observation of coherent interorbital spin-exchange dynamics, Phys. Rev. Lett. **113**, 120402 (2014).

[15] Z. Chen, T. Tang, J. Austin, Z. Shaw, L. Zhao, and Y. Liu, Quantum quench and nonequilibrium dynamics in lattice-confined spinor condensates, Phys. Rev. Lett. **123**, 113002 (2019).

[16] M.-Z. Huang, J. A. de la Paz, T. Mazzoni, K. Ott, P. Rosenbusch, A. Sinatra, C. L. Garrido Alzar, and J. Reichel, Observing spin-squeezed states under spin-exchange collisions for a second, PRX Quantum **4**, 020322 (2023).

[17] J. Ma, X. Wang, C. Sun, and F. Nori, Quantum spin squeezing, Phys. Rep. **509**, 89 (2011).

[18] L. Pezzè, A. Smerzi, M. K. Oberthaler, R. Schmied, and P. Treutlein, Quantum metrology with nonclassical states of atomic ensembles, Rev. Mod. Phys. **90**, 035005 (2018).

[19] B. Lücke, M. Scherer, J. Kruse, L. Pezzé, F. Deuretzbacher, P. Hyllus, O. Topic, J. Peise, W. Ertmer, J. Arlt, L. Santos, A. Smerzi, and C. Klempt, Twin matter waves for interferometry beyond the classical limit, Science **334**, 773 (2011).

[20] Q. Liu, L.-N. Wu, J.-H. Cao, T.-W. Mao, X.-W. Li, S.-F. Guo, M. K. Tey, and L. You, Nonlinear interferometry beyond classical limit enabled by cyclic dynamics, Nat. Phys. **18**, 167 (2022).

[21] J. Dalibard, F. Gerbier, G. Juzeliūnas, and P. Öhberg, *Colloquium*: Artificial gauge potentials for neutral atoms, Rev. Mod. Phys. **83**, 1523 (2011).

[22] B. Gadway, D. Pertot, R. Reimann, and D. Schneble, Superfluidity of interacting bosonic mixtures in optical lattices, Phys. Rev. Lett. **105**, 045303 (2010).

[23] A. V. Yulin, Y. V. Bludov, V. V. Konotop, V. Kuzmiak, and M. Salerno, Superfluidity of Bose-Einstein condensates in toroidal traps with nonlinear lattices, Phys. Rev. A **84**, 063638 (2011).

[24] T. Kovachy, P. Asenbaum, C. Overstreet, C. A. Donnelly, S. M. Dickerson, A. Sugarbaker, J. M. Hogan, and M. A. Kasevich, Quantum superposition at the half-metre scale, Nature (London) **528**, 530 (2015).

[25] F. Anders, A. Idel, P. Feldmann, D. Bondarenko, S. Loriani, K. Lange, J. Peise, M. Gersemann, B. Meyer-Hoppe, S. Abend, N. Gaaloul, C. Schubert, D. Schlippert, L. Santos, E. Rasel, and C. Klempt, Momentum entanglement for atom interferometry, Phys. Rev. Lett. **127**, 140402 (2021).

[26] S. A. Moses, J. P. Covey, M. T. Miecnikowski, D. S. Jin, and J. Ye, New frontiers for quantum gases of polar molecules, Nat. Phys. **13**, 13 (2017).

[27] J. L. Bohn, A. M. Rey, and J. Ye, Cold molecules: Progress in quantum engineering of chemistry and quantum matter, Science **357**, 1002 (2017).

[28] I. Bloch, J. Dalibard, and W. Zwerger, Many-body physics with ultracold gases, Rev. Mod. Phys. **80**, 885 (2008).

[29] S. Giorgini, L. P. Pitaevskii, and S. Stringari, Theory of ultracold atomic Fermi gases, Rev. Mod. Phys. **80**, 1215 (2008).

[30] M. He, C. Lv, and Q. Zhou, Losses, many-body correlations, and universality in ultracold molecules, Adv. Quantum Technol. **5**, 2100117 (2022).

[31] E. M. Bookjans, C. D. Hamley, and M. S. Chapman, Strong quantum spin correlations observed in atomic spin mixing, Phys. Rev. Lett. **107**, 210406 (2011).

[32] A. Perrin, H. Chang, V. Krachmalnicoff, M. Schellekens, D. Boiron, A. Aspect, and C. I. Westbrook, Observation of atom pairs in spontaneous four-wave mixing of two colliding Bose-Einstein condensates, Phys. Rev. Lett. **99**, 150405 (2007).

[33] J.-C. Jaskula, M. Bonneau, G. B. Partridge, V. Krachmalnicoff, P. Deuar, K. V. Kheruntsyan, A. Aspect, D. Boiron, and C. I. Westbrook, Sub-Poissonian number differences in four-wave mixing of matter waves, Phys. Rev. Lett. **105**, 190402 (2010).

[34] L. Deng, E. Hagley, J. Wen, M. Trippenbach, Y. Band, P. Julienne, J. Simsarian, K. Helmerson, S. Rolston, and W. Phillips, Four-wave mixing with matter waves, Nature (London) **398**, 218 (1999).

[35] J. M. Vogels, K. Xu, and W. Ketterle, Generation of macroscopic pair-correlated atomic beams by four-wave mixing in Bose-Einstein condensates, Phys. Rev. Lett. **89**, 020401 (2002).

[36] D. Pertot, B. Gadway, and D. Schneble, Collinear four-wave mixing of two-component matter waves, Phys. Rev. Lett. **104**, 200402 (2010).

[37] W. RuGway, S. S. Hodgman, R. G. Dall, M. T. Johnsson, and A. G. Truscott, Correlations in amplified four-wave mixing of matter waves, Phys. Rev. Lett. **107**, 075301 (2011).

[38] K. M. Hilligsøe and K. Mølmer, Phase-matched four wave mixing and quantum beam splitting of matter waves in a periodic potential, Phys. Rev. A **71**, 041602(R) (2005).

[39] N. Gemelke, E. Sarajlic, Y. Bidel, S. Hong, and S. Chu, Parametric amplification of matter waves in periodically translated optical lattices, Phys. Rev. Lett. **95**, 170404 (2005).

[40] G. K. Campbell, J. Mun, M. Boyd, E. W. Streed, W. Ketterle, and D. E. Pritchard, Parametric amplification of scattered atom pairs, Phys. Rev. Lett. **96**, 020406 (2006).

[41] M. Bonneau, J. Ruaudel, R. Lopes, J.-C. Jaskula, A. Aspect, D. Boiron, and C. I. Westbrook, Tunable source of correlated atom beams, Phys. Rev. A **87**, 061603(R) (2013).

[42] T. Wasak, V. V. Konotop, and M. Trippenbach, Atom laser based on four-wave mixing with Bose-Einstein condensates in nonlinear lattices, Phys. Rev. A **88**, 063626 (2013).

[43] D. McKay and B. DeMarco, Thermometry with spin-dependent lattices, New J. Phys. **12**, 055013 (2010).

[44] K. Wen, Z. Meng, L. Wang, L. Chen, L. Huang, P. Wang, and J. Zhang, Experimental study of tune-out wavelengths for spin-dependent optical lattice in ^{87}Rb Bose-Einstein condensation, J. Opt. Soc. Am. B **38**, 3269 (2021).

[45] Y. B. Ovchinnikov, J. H. Müller, M. R. Doery, E. J. D. Vredenbregt, K. Helmerson, S. L. Rolston, and W. D. Phillips, Diffraction of a released Bose-Einstein condensate by a pulsed standing light wave, Phys. Rev. Lett. **83**, 284 (1999).

[46] B. Gadway, D. Pertot, R. Reimann, M. G. Cohen, and D. Schneble, Analysis of Kapitza-Dirac diffraction patterns beyond the Raman-Nath regime, Opt. Express **17**, 19173 (2009).

[47] M. Trippenbach, Y. B. Band, and P. S. Julienne, Theory of four-wave mixing of matter waves from a Bose-Einstein condensate, Phys. Rev. A **62**, 023608 (2000).

[48] J. P. Burke, P. S. Julienne, C. J. Williams, Y. B. Band, and M. Trippenbach, Four-wave mixing in Bose-Einstein condensate systems with multiple spin states, Phys. Rev. A **70**, 033606 (2004).

[49] K. M. Mertes, J. W. Merrill, R. Carretero-González, D. J. Frantzeskakis, P. G. Kevrekidis, and D. S. Hall, Nonequilibrium dynamics and superfluid ring excitations in binary Bose-Einstein condensates, Phys. Rev. Lett. **99**, 190402 (2007).

[50] M. Egorov, B. Opanchuk, P. Drummond, B. V. Hall, P. Hannaford, and A. I. Sidorov, Measurement of *s*-wave scattering lengths in a two-component Bose-Einstein condensate, Phys. Rev. A **87**, 053614 (2013).

[51] H. Shim and T. Bergeman, Phase coherence and fragmentation of two-component Bose-Einstein condensates loaded in state-dependent optical lattices, Phys. Rev. A **94**, 043631 (2016).